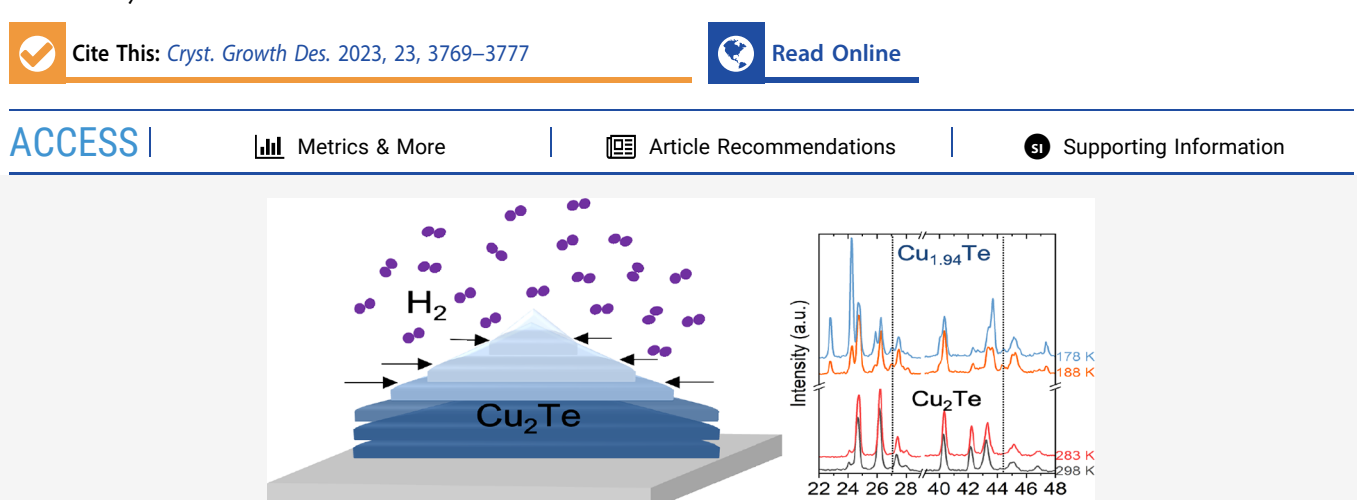


pubs.acs.org/crystal Article

Understanding the Dynamic Liquid-Assisted Chemical Vapor Deposition Growth of Copper Telluride and Its Low-Temperature Phase Transition

Yea-Shine Lee, Dmitry Lebedev, Eric K. Qian, Paloma Lee, Mercouri G. Kanatzidis, Mark C. Hersam, and Vinayak P. Dravid*



ABSTRACT: Copper telluride is an emerging layered material that has been shown to undergo phase transitions with slight modifications in its stoichiometry ($Cu_{2-x}Te$) at high temperatures. Using Raman spectroscopy and X-ray diffraction, we complete the spectrum of temperatures and detect a low-temperature phase transition of copper telluride for the first time. Moreover, liquid-assisted chemical vapor deposition (CVD) growth is heavily explored for its potential to grow various crystals at a large scale. However, the role that the liquid precursor plays in these growths remains largely elusive, and a theoretical study is impeded by the bulk amorphous liquid precursor. Here, we experimentally demonstrate how the liquid precursor contributes to the morphological orientations of $Cu_{0.664}Te_{0.336}$ crystals. Based on this, we propose a growth process in which tellurium supersaturation of the liquid precursor yields nucleation sites both on the surface and internally. Etching of $Cu_{0.664}Te_{0.336}$ via H_2 flow is also achieved during CVD to increase the density of exposed sites. Optimal parameters to control H_2 flow to achieve layer-by-layer thinning in geometric crystals are also realized. Our study thereby enhances the understanding of temperature-dependent copper telluride phases and presents liquid-assisted growth as a platform ripe with opportunities for materials engineering.

1. INTRODUCTION

The capability to grow at a large scale with controllable thickness is of great merit in layered materials as it enables adoption in nanoscale devices at the industrial level. 1-4 Many have explored an unconventional chemical vapor deposition (CVD) technique of using liquid precursors in an effort to achieve this with traditional two-dimensional (2D) materials such as transition metal dichalcogenides. 2,3,5-7 However, another layered material that can potentially reap the benefits of liquid-assisted CVD growth is copper telluride (Cu_{2-x}Te). This is an emerging layered material with promising applications in thermoelectrics and lithium ion batteries.^{8–12} For example, $Cu_{0.664}Te_{0.336}$ (PDF no. 00-037-1027) has been investigated as photocathodes in water splitting applications¹³ and lasing and surface-enhanced Raman spectroscopy (SERS) applications. 14 Air stability further positions copper telluride as an attractive candidate for continued active research. 15 Despite

such work, large-scale synthesis techniques of copper telluride have been largely overlooked.

Previously, we reported a unique liquid-assisted copper chalcogenide synthesis technique in which chalcogen vapor diffuses into and supersaturates the molten copper foil sandwiched between tungsten foil and a sapphire substrate before crystallization.⁶ The use of molten copper in this technique is noteworthy because (1) it is an amorphous precursor with no predetermined preferential nucleation site, (2) it is in significant excess relative to the chalcogen, and (3) by nature of being molten, it forms a droplet morphology on

Received: February 13, 2023 Revised: March 20, 2023 Published: April 10, 2023





Crystal Growth & Design pubs.acs.org/crystal Article

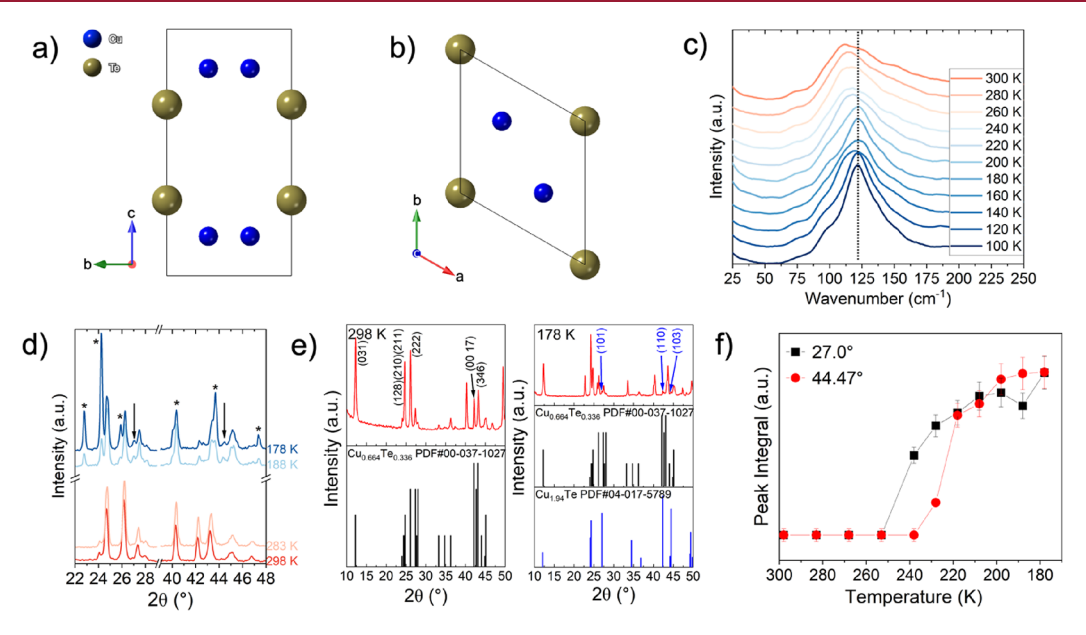


Figure 1. Low-temperature transition of copper telluride. P6/mmm Cu₂Te structure, of which the orthorhombic Cu_{0.664}Te_{0.336} is a superstructure, viewed from (a) a-axis and (b) c-axis. (c) Low-temperature Raman spectra showing a shift in the most intense peak position between 200 and 220 K as outlined by the dashed line. (d) Low-temperature GIXRD patterns at 298, 283, 188, and 178 K with new peaks at 27.0 and 44.47° marked with arrows. Peaks due to substrates and the setup are marked with "*". (e) GIXRD pattern of copper telluride at 298 K indexed to Cu_{0.664}Te_{0.336} (PDF no. 00-037-1027) and at 178 K indexed to a combination of Cu_{0.664}Te_{0.336} (PDF no. 00-037-1027) and Cu_{1.94}Te (PDF no. 04-017-5789). The most intense peaks from Cu_{1.94}Te are marked in blue arrows. (f) Intensities of the 27.0 and 44.47° peaks from Cu_{1.94}Te increase with decreasing temperature first detected at 238 and 228 K, respectively, suggesting a phase transition.

the substrate. These conditions result in large amounts of amorphous excess copper and some crystals that grow on the curved surface of the droplet. Moreover, this synthesis yields crystals that are several micrometers thick with lateral coverage on the millimeter scale. Some exfoliation is achieved by mechanically peeling the two substrates from one another after growth, though this produces nonuniform, random exfoliation. As calculations on the amorphous, liquid precursors are challenging, systematic experimentation is the key to understand the underlying growth process. Moreover, ways to modulate the crystal thickness to obtain desirable copper telluride crystals are still needed.

Efforts to expand the functionality of layered materials have included increasing the density of chemically reactive sites by introducing defects or etching 15–19 and achieving vertical growth to expose reactive edge sites. 20,21 These have implications for catalysis. In particular, copper plays a prominent role in many modern catalytic reactions such as aerobic oxidation reactions, 2 hydrogenation reactions, 3 and CO₂ electroreduction reactions. The abundance of copper sites in copper telluride inherently makes this material a promising candidate for catalysis. For instance, Han *et al.* reported the electrocatalytic property of Cu₂Te nanostructures as counter electrodes of quantum dot-sensitized solar cells. Hence, the ability to induce etching or achieve a standing morphology of copper telluride is highly desirable.

Moreover, understanding phase transitions of materials is critical for adoption in various applications. For example, materials that undergo temperature-induced phase transformations have diverse applications in nanoelectronics and information storage technologies. Zhang *et al.* have reported multiple reversible high-temperature phase transitions of copper telluride that begin from 150 °C. Not only does this directly affect phonon scattering and carrier scattering for thermoelectric applications but also determines the limits of

high-performance devices. While high-temperature phase transitions have been investigated and the phase diagram of copper telluride at high temperatures is well-known with the $Cu_{0.664}Te_{0.336}$ phase stable at near 450 K, ^{29–31} its behavior at temperatures below room temperature has not yet been reported.

Herein, we bring the copper telluride crystals to a temperature as low as 100 K for the first time to reveal that the orthorhombic Cu₂Te (Cu_{0.664}Te_{0.336} PDF no. 00-037-1027)13,14 can remain stable until near 220 K, at which point a phase transition to hexagonal Cu_{1.94}Te (PDF no. 04-017-5789) occurs. Next, we pave the way for realizing the role of the liquid precursor in deriving standing (and tilted) $\text{Cu}_{0.664}\text{Te}_{0.336}$ morphologies via liquid-assisted CVD growth. Such an experimental understanding is critical as an amorphous liquid precursor impedes a theoretical approach. We then systematically vary temperature and time to pinpoint how H₂ gas during growth can simultaneously etch the $Cu_{0.664}Te_{0.336}$ crystals. Optimal parameters for etching such that chemical thinning of the bulk crystal is achieved are also identified. This is promising in the field of nanoelectronics as it leaves thin crystals in a one-step method with minimal residue associated with conventional mechanical exfoliation of layered materials.

2. EXPERIMENTAL METHODS

2.1. Synthesis. Double-side polished Cu foil (Alfa Aesar, 99.5% purity, $\sim 10~\mu m$ thick) cut to $5\times 5~mm^2$ was sandwiched between an Al $_2$ O $_3$ sapphire substrate and W foil (Alfa Aesar, 99.99% purity, $\sim 100~\mu m$ thick) of similar dimensions and placed in an alumina crucible at the center of a tube (fused quartz; inner diameter of 22 mm, outer diameter of 25 mm) furnace (Lindberg Blue M). Twelve milligrams of Te powder (Alfa Aesar, 99.9999% metal basis) was placed in a separate alumina crucible and placed 10 cm upstream from the first crucible (Figure S1). Under 140 sccm Ar and 10 sccm H $_2$, the center of the furnace was heated from room temperature to 1085 °C at 21.3 °C/min then held at 1085 °C for 30 min for growth. Then, H $_2$ was

Crystal Growth & Design pubs.acs.org/crystal Article

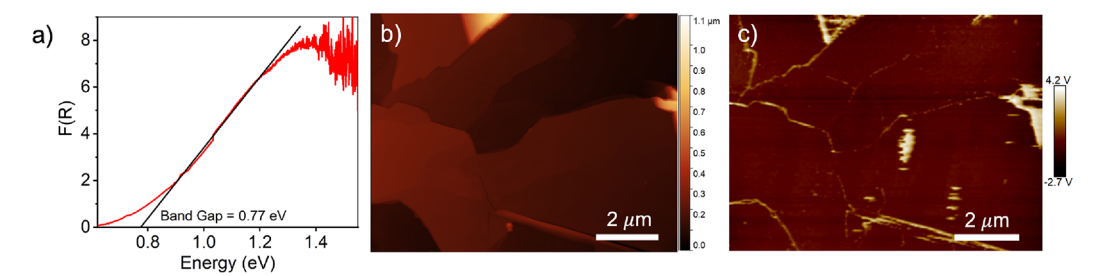


Figure 2. Electronic behavior of $Cu_{0.664}Te_{0.336}$. (a) $Cu_{0.664}Te_{0.336}$ is a semiconductor with a band gap of 0.77 eV measured by UV–Vis spectroscopy. (b) Topography of $Cu_{0.664}Te_{0.336}$. (c) Corresponding surface potential shows a higher surface potential at the boundaries than in the interior, implying that the bulk is not conductive in contrast to the boundary.

cut off, and the furnace underwent a natural cool down to 400 $^{\circ}\mathrm{C}$ at which point the furnace was opened and samples were quenched.

2.2. Characterization. Optical images of grown samples were taken with a Nikon Ci POL microscope system.

A Horiba LabRam confocal Raman system equipped with an HJY detector was used to collect Raman spectra in ambient conditions. A 473 nm laser with 1800 gr/mm grating and 10% ND filter was used.

Low-temperature Raman spectra were collected using a Horiba XPloRA confocal setup (473 nm laser with 2400 gr/mm grating and 10% ND filter, 50× long working distance objective) equipped with a Linkam stage. The sample was pumped down with a roughing pump and cooled using a flow of liquid N_2 .

A Bruker ICON AFM system was used in the tapping mode in air at a scan rate of $1\ \mathrm{Hz}$.

A Bruker photocurrent and thermal AFM system was used in the lift mode in air at a scan rate of 0.3 Hz.

The secondary electron mode of an SEM Hitachi SU8030 system was operated at 10 kV. The instrument was equipped with an Oxford Aztec X-max 80 SDD EDS detector.

TEM samples were prepared by a polystyrene-assisted transfer technique. ³² The sapphire substrate with copper telluride crystals was spin-coated with a solution of 9 g of polystyrene (280,000 g/mol) in 100 mL of toluene at 4000 rpm for 45 s. Then, the substrate was baked at 80 °C for 15 min. Next, Cu₂Te on polystyrene was delaminated from sapphire upon contact with water, and a Ni TEM grid was used to lift the film from the water. Finally, the TEM grid with the film was baked at 80 °C for 1 h and 150 °C for 30 min. The polymer was then washed away with toluene. TEM images were obtained using a probe-corrected JEOL ARM200CF microscope operated at 200 kV.

The low-temperature crystal structures were indexed by a Rigaku SmartLab out-of-plane grazing incidence angle XRD instrument using Cu K α radiation. The instrument has the capability to measure down to 173 K. Measurements were conducted in vacuum under a polyether ether ketone (PEEK) dome, and crystals on the W substrate were used for measurement.

The UV–Vis–NIR spectrum in the transmittance mode was collected at room temperature using a Cary 5000 UV–Vis–NIR double-beam spectrophotometer with a monochromator. An empty sapphire substrate was used as a reference for the baseline collection. Transmittance data were in-software using the Kubelka–Munk equation $\alpha/S = (1-R)2/2R$, where α and S are the absorption and scattering coefficients, respectively, and R is the reflectance.

3. RESULTS AND DISCUSSION

We begin with probing the low-temperature transformation of liquid-assisted chemical vapor deposition (CVD)-grown copper telluride. The detailed discussion on growth is provided later in the section. Energy-dispersive X-ray spectroscopy (EDS) on a scanning electron microscope (SEM) indicates the \sim 2:1 copper-to-tellurium stoichiometry of grown copper telluride (Figure S2). The room-temperature Raman spectrum is in agreement, with modes at 75 and 116 cm⁻¹ attributed to

the B_{3g} and B_1 modes of the orthorhombic Cu_2Te , respectively (Figure 1c). ¹⁴ As expected, the peaks sharpen with decreasing temperature, but more notably, the most intense peak shifts significantly between 200 and 220 K to 121 cm⁻¹. Although this alone suggests a structural transformation, we further conduct low-temperature out-of-plane grazing incidence X-ray diffraction (GIXRD) to better identify the structural change.

In order to perform low-temperature GIXRD on a large area of pristine crystals, measurements are taken directly on crystals on the substrate. On the substrate, concentrations of excess copper precursor remain. The peaks from the substrate and setup, many of which appear from 188 K, are marked with "*" in Figure 1d. Indexing of the patterns at the starting and final temperatures of 298 and 178 K is shown in Figure 1e. At 298 K, the diffraction pattern can be indexed to Cu_{0.664}Te_{0.336} (PDF no. 00-037-1027). The layered orthorhombic Cu_{0.664}Te_{0.336} is a superstructure of the hexagonal structure $(P6/mmm a_0 = 4.237 \text{ Å}, c_0 = 7.274 \text{ Å})$ with lattice parameters a = $3a_0$ = 7.319 Å, b = $33a_0$ = 22.236 Å, and c = $5c_0$ = 36.458 Å.^{13,14,31} At 178 K, the pattern can be additionally indexed to the hexagonal $Cu_{1.94}$ Te (PDF no. 04-017-5789; a = 4.267 Å, c= 7.317 Å), suggesting that the orthorhombic superstructure is being reduced. The (101), (110), and (103) peaks at 178 K from Cu_{1,94}Te are marked with blue arrows in Figure 1e.

In particular, the new peaks at 27.0 and 44.47° corresponding to the (101) and (103) planes are two of the strongest diffraction peaks in Cu_{1.94}Te, which explains why they are the first to appear at the initial stages of the phase transition. The peak integral measurements shown in Figure 1f indicate that the peak at 27.0° begins to appear near 238 K while that at 44.47° begins to appear near 228 K. The complete patterns and magnified views of these peaks are in Figures S3. Therefore, the phase transition temperature is consistent between Raman spectroscopy and GIXRD, indicating that $Cu_{0.664}Te_{0.336}$ remains stable at temperatures near 220 K before beginning to form a hexagonal phase. Cycles of heating and cooling demonstrate that this phase transition is in fact nonreversible, and the two characteristic peaks remain visible at room temperature after cooling (Figure S4). Understanding such noteworthy behavior of copper telluride at low temperatures is crucial for determining the suitability of certain phases of copper telluride for low-temperature applications.

To further characterize $Cu_{0.664}Te_{0.336}$, we measure its band gap of 0.77 eV (Figure 2a), in agreement with the room-temperature orthorhombic Cu_2Te being reported as a p-type semiconductor.³³ Interestingly however, Kelvin probe force microscopy (KPFM) indicates that crystal edges may be minority carrier traps.^{34–36} A higher surface potential at the

Crystal Growth & Design pubs.acs.org/crystal Article

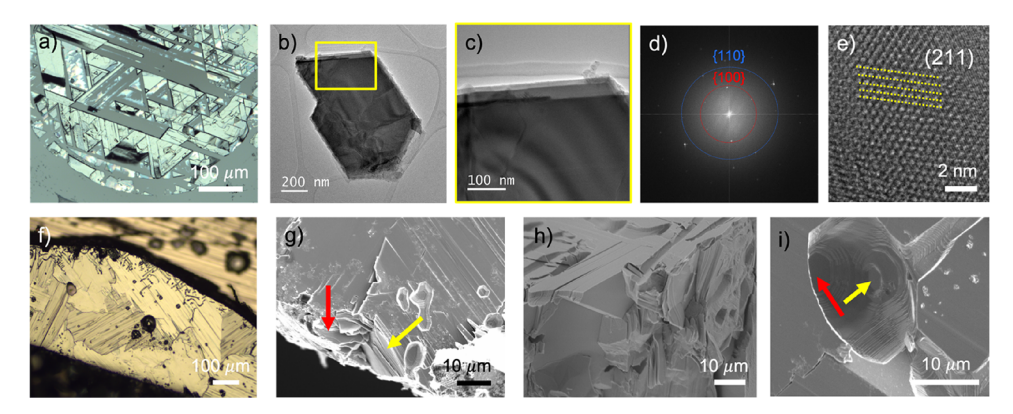


Figure 3. Optical and SEM images of $Cu_{0.664}Te_{0.336}$ crystals. (a) Optical image of oriented, geometric $Cu_{0.664}Te_{0.336}$ crystals on sapphire. (b) TEM image of a transferred crystal flake. (c) Magnified TEM image of the boxed region in (b) with (d) FFT (scale of 2 nm⁻¹) showing high crystallinity and purity. (e) HRTEM image showing five planes in a grain with an interplanar spacing of 0.362 nm corresponding to (211) planes. (f) Optical image of an island of variously oriented Cu_2 Te crystals on tungsten. (g) SEM image of variously oriented $Cu_{0.664}Te_{0.336}$ crystals showing the presence of horizontally stacked crystals (red arrow) and vertically standing crystals (yellow arrow). (h) SEM image of a cross section showing the presence of crystal stacking at various orientations. (i) SEM image of the $Cu_{0.664}Te_{0.336}$ surface showing in-plane etching in hexagonal trenches. Etching of horizontally stacked crystals (red arrow) and vertically stacked crystals (yellow arrow) is outlined.

edges compared to the interior as demonstrated in Figure 2b,c suggests a downward potential bending at the edges, which enhances carrier separation. This not only contributes to the conductivity of the material but is promising as it suggests that electron—hole recombination can be suppressed. A similar phenomenon has been reported in the Cu_{2-x}Te weissite structure where the grain boundaries show a higher surface potential than the interior.

Next, we experimentally investigate the liquid-assisted CVD growth process of Cu_{0.664}Te_{0.336} to understand key factors in this growth process and explore parameters to engineer Cu_{0.664}Te_{0.336}. The crystals are grown as tellurium vapor supersaturates the molten copper foil inside a hot tube furnace (see Experimental Methods). The copper foil is sandwiched between a piece of tungsten foil below and a piece of sapphire above as shown in Figure S2 and described by Shehzad *et al.*⁶ and Feng *et al.*⁷ As the copper foil melts, several distinct droplets form, each of which reacts with tellurium to yield a few islands of bulk Cu_{0.664}Te_{0.336} crystals. Having substrates above and below the molten copper not only prevents the copper from dewetting⁶ but also assists with epitaxially orienting the crystals that grow in contact with the *c*-plane surface of sapphire as shown in Figure 3a.³⁷

A polystyrene-assisted transfer technique from the sapphire substrate preserves the geometry of the crystals upon transfer to a transmission electron microscope (TEM) grid, as seen in Figure 3b. A magnified view of the boxed region is shown in Figure 3c with the corresponding fast Fourier transform (FFT) pattern of a single set of six-fold symmetry in Figure 3d demonstrating high crystallinity and phase purity. An interplanar spacing of 0.362 nm is measured on the high-resolution TEM (HRTEM) in-plane image in Figure 3e, which is in good agreement with the reported interplanar spacing of 0.359 nm of the (211) planes 13 of $\mathrm{Cu}_{0.664}\mathrm{Te}_{0.336}$ and validates the phase identified by GIXRD and Raman spectroscopy. The (211) plane is a highly preferred plane forming the basal layers in $\mathrm{Cu}_{0.664}\mathrm{Te}_{0.336}$.

In contrast to the crystals that grow in contact with the sapphire substrate, those that grow in contact with the tungsten substrate are uniquely patch-like (Figure 3f), lacking the geometric outlines found on the sapphire substrate. A SEM image of such a region marked by a yellow arrow in Figure 3g

reveals standing, vertically stacked layers of $Cu_{0.664}Te_{0.336}$. This is unlike the classic horizontally stacked layers of $Cu_{0.664}Te_{0.336}$ marked by a red arrow in Figure 3g. The role of the liquid precursor is highlighted here: variously oriented crystals grow on the polycrystalline tungsten substrate due to the molten liquid nature of the precursor, a bulk amorphous material with no preferred orientation. Because the tellurium vapor does not necessarily prefer saturating the surface over the internal bulk of molten copper, it is possible that nucleation occurs randomly and growth occurs in nonhorizontal orientations in the bulk. This is further supported by panel h, a SEM image of a cross section of Cu_2Te bulk growth. As expected, stacking of layers is not only limited to the vertical and horizontal directions but also includes directions that range in between (i.e., tilted).

The nonspecific nucleation sites and directions of the first monolayer growth within the amorphous copper likely determine the stacking orientation on the tungsten substrate, unlike that on the sapphire substrate. Next, in-plane growth and subsequent layering continue until a stack of layers intersects in different orientations. The use of molten liquid bulk precursors on polycrystalline substrates for layered crystal growth thereby offers a platform to yield crystals of various orientations. This has implications in catalysis or example, where the exposed edge sites are reactive sites, and standing or tilted stacking of layers offers an abundance of accessible edge sites.

Reactive edge sites can be further induced on the surface of $Cu_{0.664}Te_{0.336}$ crystals similarly on both substrates as shown in Figure 3i. Continuous flow of Ar and H_2 gas after growth completion renders an ongoing reaction within the isolated system. The direction of etching aligns with the orientation of the multilayer $Cu_{0.664}Te_{0.336}$ stacks. The hexagonal trenches follow the crystal stacking orientation: they etch in-plane at all times. The red arrow in Figure 3i points toward vertical etching in horizontally stacked crystal layers, while the yellow arrow points to lateral etching in vertically stacked layers. Understanding that flowing H_2 gas throughout the synthesis is inducing the etching, it is important to note that there may be a dynamic interplay between etching and growth where a precursor material compensates for etching during the high-temperature growth. ¹⁵ To modulate the etching behavior, we

further systematically vary three parameters: gas, temperature, and time.

The density of etching on Cu_{0.664}Te_{0.336} is the highest on the edges of bulk crystals, suggesting that it is due to gas presence following growth. In addition to hydrogen, 18 oxygen 16,41 and water vapor 17,40 are chosen for inspection since they are not only common etchants but also possibly present in trace amounts within the synthesis tube system. If a gas is an etchant, then exposing the as-grown $Cu_{0.664}Te_{0.336}$ to an excess amount of this gas should enhance etching. First, the as-grown $Cu_{0.664}Te_{0.336}$ is annealed in O_2 for 30 min at 300, 700, and 1000 °C. At all temperatures, the crystals are significantly degraded, and the crystal surface is covered by CuO as confirmed by Raman spectroscopy and EDS (Figure S5). Even upon annealing in ambient conditions, where there is more water vapor than in the closed reaction furnace tube, CuO covers the surface and etching that was present prior to annealing is no longer visible (Figure S5).

Next, the effect of H_2 is considered. During $Cu_{0.664}Te_{0.336}$ growth, 10 sccm H_2 is kept flowing at 1085 °C in order to activate the copper surface. Cutting H_2 flow prematurely at 0, 15, and 30 min into growth results in similar levels of etching (Figure S6). In particular, cutting off H_2 before growth begins (0 min) yields large areas of unreacted copper, underscoring the importance of H_2 in activating the copper surface prior to nucleation.

On the other hand, different durations of H_2 flow after the growth is complete have significant effects on etching as summarized in Table 1. Annealing in 10 sccm H_2 at 1000 °C

Table 1. $Cu_{0.664}Te_{0.336}$ Crystal Product by Annealing in 140 sccm Ar and 10 sccm H_2 Flow at Different Temperatures and Durations

annealing temperature (°C)	annealing time (min)	crystal product
1080	10	Crystals severely damaged; morphology is unrecognizable. (Figure S10)
1000	30	Extreme etching; only excess copper base remains.
1000	10	Moderate etching; some excess copper base exposed and visibly darker crystal grain boundaries.
900	30	Moderate etching; increased amounts of trenches and visibly darker crystal grain boundaries.
900	10	Mild etching; crystals are thinned layer-by-layer.

for 30 min aggressively etches the crystals such that all $Cu_{0.664}Te_{0.336}$ crystals are eliminated and only excess copper at the base of the crystals remains (Figure 4a,b). The crystals are in green and copper is in yellow in the optical images. Upon shortening the annealed time to 10 min, there is noticeably less etching. The majority of the $Cu_{0.664}Te_{0.336}$ crystals remain recognizable (Figure 4c,d). With this shorter annealing duration, crystal etching is most prominent in regions near the excess copper where the $Cu_{0.664}Te_{0.336}$ edges are likely incomplete and thus chemically reactive. Similarly, grain boundaries often host defects and edge sites that facilitate etching and appear darker in the optical image (Figure 4d) after annealing. Raman spectroscopy on $Cu_{0.664}Te_{0.336}$ at the etched region demonstrates that etching does not alter the crystal structure (inset of Figure 4d).

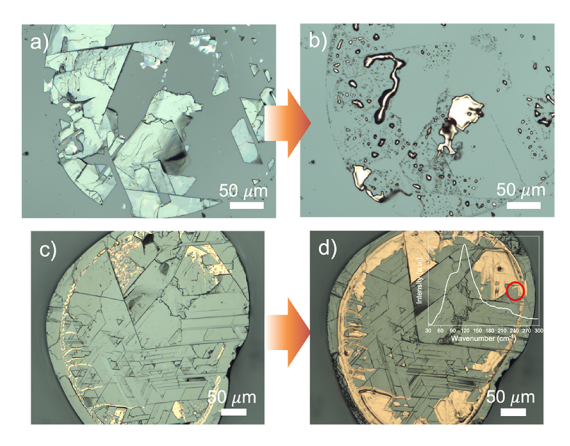


Figure 4. Optical images of $Cu_{0.664}Te_{0.336}$ crystals before and after annealing in an Ar/H_2 environment at 1000 °C. Optical images of $Cu_{0.664}Te_{0.336}$ crystals prior to annealing for (a) 30 and (c) 10 min. (b) Optical image of $Cu_{0.664}Te_{0.336}$ crystals in (a) after annealing shows severe degradation of crystals with only excess copper base remaining. (d) Optical image of $Cu_{0.664}Te_{0.336}$ crystals in (c) after annealing shows moderate etching exposing some excess copper base and darker grain boundaries. Inset: Raman spectrum of the etched region marked with a red circle in (d). The Raman spectrum shows no change, indicating that etching does not alter the crystal structure.

Annealing $Cu_{0.664}Te_{0.336}$ in 10 sccm H_2 at a lower temperature of 900 °C for 30 min also increases the density of trenches on the crystal surface as shown in Figure 5a,b. The SEM image of these crystals in Figure 5e illustrates grooves at grain boundaries as a result of etching pointed out by red arrows. However, at this temperature, no regions are completely etched to the point where only excess copper remains.

Refined Cu_{0.664}Te_{0.336} annealing is finally achieved at a temperature of 900 °C held for 10 min. Rather than forming hexagonal trenches on the surface, the bulk Cu_{0.664}Te_{0.336} crystals are thinned in a layer-by-layer manner under these conditions. Figure 5c,d shows optical images of crystals before and after annealing at 900 °C held for 10 min. The as-grown bulk crystals typically have a wide thickness range of hundreds of nanometers (Figure S7) due to the random nature of exfoliation upon peeling the two substrates after liquid-assisted growth. After annealing, crystal thinning is observed rather than hexagonal trenches. An annealed region is analyzed with atomic force microscopy (AFM) in Figure 5f. All triangular grains are oriented in the same direction as expected on the sapphire substrate. Most crystals are thinned by an order of magnitude and range tens of nanometers thick as shown by the line profile insets. A crystal of thickness of ~1.44 nm can also be achieved with refined annealing as shown in Figure S7. The line profile insets in Figure 5f illustrate the layered steps revealed from the thinned crystal. There is a small range of annealed crystal thickness due to the variation in the starting thickness; however, the H₂ etching technique is evidently robust to any as-grown crystal thicknesses and can be modulated to produce both trench-type etching and layer-bylayer etching.

This liquid-assisted CVD growth is a unique technique that is advantageous for producing large areas of bulk $Cu_{0.664}Te_{0.336}$ crystals. However, achieving few-layer crystals with this growth had been previously left to chance upon peeling the two substrates. Furthermore, mechanical exfoliation had been previously limited to random smaller crystals and suffered from

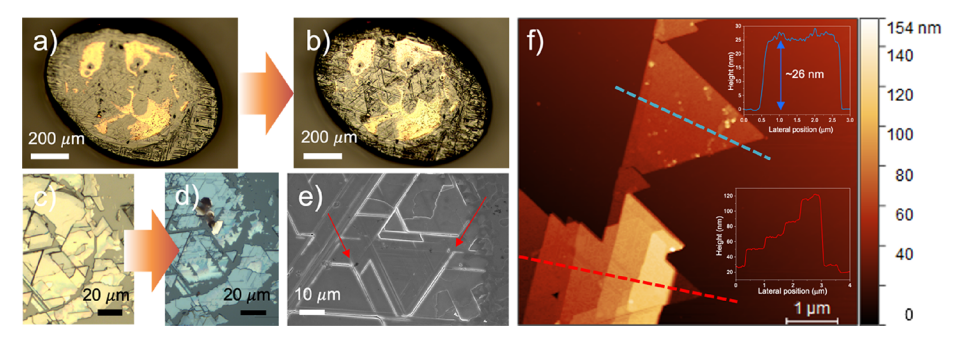


Figure 5. Images of $Cu_{0.664}Te_{0.336}$ crystals before and after annealing in an Ar/H₂ environment at 900 °C. Optical images of $Cu_{0.664}Te_{0.336}$ crystals before annealing for (a) 30 and (c) 10 min. (b) Optical image of crystals in (a) after annealing shows more etched trenches and darker outlines of geometric grains. The SEM image in (e) shows that the dark geometric outlines are likely due to preferential etching along the reactive grain boundaries as highlighted by red arrows. (d) Optical image of crystals in (c) after annealing shows mild etching in the form of crystal thinning. (f) AFM image of a sample annealed at 900 °C for 10 min illustrating that etching occurs layer-by-layer to reveal multiple triangular grain surfaces. Insets show height profiles of corresponding red and blue line profiles.

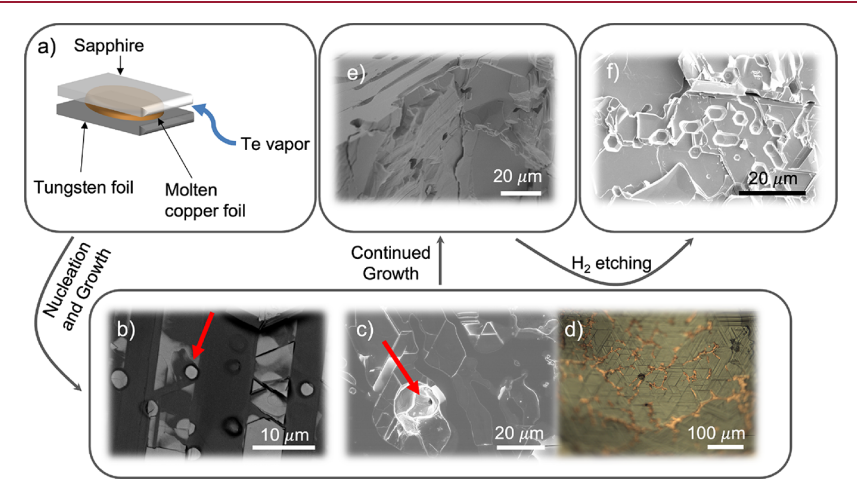


Figure 6. Proposed growth process of $Cu_{0.664}Te_{0.336}$. (a) Schematic showing the start of the reaction. Te vapor diffuses through and supersaturates the molten copper between the sapphire and tungsten foil substrates, and nucleation occurs. SEM image of growth from nucleation (b) on the surface of copper in contact with sapphire leading to epitaxial, horizontal layering and (c) within the bulk copper leading to nonhorizontal layering. (d) Optical image of $Cu_{0.664}Te_{0.336}$ crystals grown on the curved surface of a molten copper droplet, another region prone to nonhorizontal layering. (e) Cross-sectional SEM image after complete growth capturing various bulk layering orientations that intersect down the depth of the $Cu_{0.664}Te_{0.336}$ crystal. (f) SEM image showing the in-plane $Cu_{0.664}Te_{0.336}$ crystals with hexagonally etched trenches from H_2 gas flow.

residue contamination. H₂ gas annealing postgrowth offers a controllable and one-step method to chemically engineer the surface morphology and the thickness. We propose that at milder temperatures and shorter durations, the top layer is etched away beginning from the grain boundaries, the largest and most accessible reactive site. Then, the underlying layer is etched away from the exposed grain boundaries, and thinning proceeds layer-by-layer in this manner. At high temperatures or longer durations, new point defects can be induced in-plane, and existing defects can become mobile and aggregate. These become attractive high-energy reactive sites that are predisposed toward trench formation.

Annealing in H_2 also thins bulk $Cu_{0.664}Te_{0.336}$ crystals transferred onto silicon wafers (300 nm native oxide layer), substrates that are industrially adopted. Transferred crystals have an average thickness near 60 nm, and annealing in H_2 for 5 min reduces the average thickness to near 8 nm, suggesting a thinning rate of 1.7 Å/s as shown in Figure S7. However, the mechanical transfer technique deposits a residue as shown by small spherical bumps on the crystal surface, and the residue hinders thinning (Figure S8). Thus, more work is required to

minimize residue deposition during transfer in order to obtain clean layer-by-layer thinning on transferred crystals.

To further comprehend the liquid-assisted growth, we begin with an analysis of the substrate of choice. Upon performing the synthesis with two tungsten foil substrates, we confirm the absence of both preferential orientation of crystals and large-area geometric crystals (Figure S9). In contrast, using two sapphire substrates yields oriented, large-area triangular crystals (Figure S9) confirming the epitaxial behavior offered on sapphire. Variations in the growth length from 10 to 45 min result in very sparse crystal growth with large areas of unreacted copper and large coverage with no visible excess copper, respectively, confirming more crystal growth with longer duration (Figure S9).

Combining these experimental trends, a potential holistic growth process of liquid-assisted CVD can be proposed with high confidence. First, as the tellurium vapor diffuses through the edge of the molten copper between the two substrates as depicted in Figure 6a, nucleation can occur both on the interface of molten copper and sapphire (Figure 6b), where epitaxial growth occurs, and within the bulk molten copper (Figure 6c). The region with the red arrow in Figure 6c, unlike

the surrounding region of quenched molten copper, shows much more progressed growth as nucleation likely occurred within the bulk molten copper. Many layers of Cu_{0.664}Te_{0.336} crystals are visible into the depth, and these crystals are oriented in various directions. Then, these crystals continue both in- and out-of-plane growth until obstructed by crystals of different orientations as seen in Figure 6e. Crystals of nonhorizontal stacking may also form if nucleation and growth occur on the curved edge surface of molten copper droplets. One such region is illustrated in Figure 6d. Green corresponds to Cu_{0.664}Te_{0.336} crystals, while the golden lining in between is the underlying excess copper base. The varying focus of this optical image is due to the curvature on the edge. In this case, it is evident that the crystals will layer in a nonhorizontal direction, tangential to the surface curvature. After multilayer growth, bulk crystals intersect at various orientations as shown in Figure 6e. Finally, with H₂ flow during cooling after growth, etching and thinning on the crystal surface become evident as shown in Figure 6f.

4. SUMMARY AND CONCLUSIONS

We report the structure of copper telluride at low temperatures for the first time, demonstrating that the orthorhombic $Cu_{0.664}Te_{0.336}$ superstructure remains stable from room temperature down to near 220 K before undergoing a transition to hexagonal Cu_{1.94}Te. This complements the known high-temperature phase transitions and provides a complete view of the dynamic phase transitions of copper telluride. Furthermore, we propose a likely growth process of Cu_{0.664}Te_{0.336} via the unique liquid-assisted CVD. Once tellurium diffuses through and supersaturates the molten copper precursor, nucleation favorably occurs both on the sapphire surface as well as in the bulk copper. While growth on the surface yields conventional in-plane crystals, those in the bulk can grow at a multitude of orientations. Hence, liquidassisted growth is favorable toward growing crystals at various orientations with exposed edge sites. We demonstrate that H₂ flow at high annealing temperatures can be further modulated to etch $Cu_{0.664}Te_{0.336}$ in-plane in hexagonal lattice trenches, exposing a high density of edge sites, and to thin the crystals layer-by-layer and realize few-layer Cu_{0.664}Te_{0.336}. Our work thereby deepens the understanding of the role of the liquid precursor in Cu_{0.664}Te_{0.336} growth. We also present the first steps to tunable etching as a path to improve the functionality of Cu_{0.664}Te_{0.336} in fields such as catalysis and nanoelectronics.

ASSOCIATED CONTENT

Supporting Information

The Supporting Information is available free of charge at https://pubs.acs.org/doi/10.1021/acs.cgd.3c00149.

Schematic of the growth setup, EDS of crystals, full GIXRD patterns of substrates and copper telluride at all measured temperatures, GIXRD patterns of multiple heating—cooling cycles, SEM and EDS images of Cu_{0.664}Te_{0.336} annealed in ambient and O₂ environments, optical images of Cu_{0.664}Te_{0.336} with H₂ gas flow variation during growth, optical and AFM images of Cu_{0.664}Te_{0.336} crystals before and after annealing, optical and AFM images of Cu_{0.664}Te_{0.336} grown for different durations, optical images of Cu_{0.664}Te_{0.336} grown for different durations, optical images of Cu_{0.664}Te_{0.336} annealed in H₂ at a higher

temperatures, and SEM and EDS images of growth using Ti and Ta foil (PDF)

AUTHOR INFORMATION

Corresponding Author

Vinayak P. Dravid — Department of Materials Science and Engineering and Northwestern University Atomic and Nanoscale Characterization Experimental (NUANCE) Center, Northwestern University, Evanston, Illinois 60208, United States; International Institute for Nanotechnology (IIN), Northwestern University, Evanston, Illinois 60208, United States; orcid.org/0000-0002-6007-3063; Email: v-dravid@northwestern.edu

Authors

Yea-Shine Lee — Department of Materials Science and Engineering, Northwestern University, Evanston, Illinois 60208, United States; International Institute for Nanotechnology (IIN), Northwestern University, Evanston, Illinois 60208, United States; orcid.org/0000-0002-2087-4886

Dmitry Lebedev — Department of Materials Science and Engineering, Northwestern University, Evanston, Illinois 60208, United States; orcid.org/0000-0002-1866-9234

Eric K. Qian – Department of Chemistry, Northwestern University, Evanston, Illinois 60208, United States

Paloma Lee – Department of Materials Science and Engineering, Northwestern University, Evanston, Illinois 60208, United States

Mercouri G. Kanatzidis — Department of Chemistry, Northwestern University, Evanston, Illinois 60208, United States; © orcid.org/0000-0003-2037-4168

Mark C. Hersam – Department of Materials Science and Engineering, Department of Chemistry, and Department of Electrical and Computer Engineering, Northwestern University, Evanston, Illinois 60208, United States;
ocid.org/0000-0003-4120-1426

Complete contact information is available at: https://pubs.acs.org/10.1021/acs.cgd.3c00149

Notes

The authors declare no competing financial interest.

ACKNOWLEDGMENTS

This work was primarily supported by NSF Division of Material Research Grant DMR-1929356 (V.P.D.) with additional support provided by DMR-2003476 (M.C.H.). Lowtemperature Raman characterization was supported by the Northwestern University Materials Research Science and Engineering Center (NSF Grant DMR-1720139). This work made use of the SPID and EPIC facilities of Northwestern University's NUANCE Center, which has received support from the SHyNE Resource (NSF Grant ECCS-2025633), Northwestern's MRSEC program (NSF Grant DMR-1720139), the Keck Foundation, and the State of Illinois through IIN. This work also made use of the Jerome B. Cohen X-ray Diffraction Facility supported by the MRSEC program of the National Science Foundation (DMR-1720139) at the Materials Research Center of Northwestern University and the SHyNE Resource (NSF ECCS-2025633). This work also made use of the IMSERC Crystallography facility at Northwestern University, which has received support from the

SHyNE Resource (NSF ECCS-2025633) and Northwestern University. Y.-S.L. gratefully acknowledges support from the Ryan Fellowship and the IIN at Northwestern University.

REFERENCES

- (1) Kang, K.; Xie, S.; Huang, L.; Han, Y.; Huang, P. Y.; Mak, K. F.; Kim, C.-J.; Muller, D.; Park, J. High-Mobility Three-Atom-Thick Semiconducting Films with Wafer-Scale Homogeneity. *Nature* **2015**, *520*, *656*–*660*.
- (2) Li, S.; Lin, Y.-C.; Zhao, W.; Wu, J.; Wang, Z.; Hu, Z.; Shen, Y.; Tang, D.-M.; Wang, J.; Zhang, Q.; Zhu, H.; Chu, L.; Zhao, W.; Liu, C.; Sun, Z.; Taniguchi, T.; Osada, M.; Chen, W.; Xu, Q.-H.; Wee, A. T. S.; Suenaga, K.; Ding, F.; Eda, G. Vapour-Liquid-Solid Growth of Monolayer MoS2 Nanoribbons. *Nat. Mater.* **2018**, *17*, 535–542.
- (3) Trentler, T. J.; Hickman, K. M.; Goel, S. C.; Viano, A. M.; Gibbons, P. C.; Buhro, W. E. Solution-Liquid-Solid Growth of Crystalline III-V Semiconductors: An Analogy to Vapor-Liquid-Solid Growth. *Science* **1995**, *270*, 1791–1794.
- (4) Xu, C.; Wang, L.; Liu, Z.; Chen, L.; Guo, J.; Kang, N.; Ma, X.-L.; Cheng, H.-M.; Ren, W. Large-Area High-Quality 2D Ultrathin Mo2C Superconducting Crystals. *Nat. Mater.* **2015**, *14*, 1135–1141.
- (5) Shehzad, M. A.; Das, P. M.; Tyner, A. C.; Cheng, M.; Lee, Y.-S.; Goswami, P.; Dos Reis, R.; Chen, X.; Dravid, V. P. Synthesis of Layered vs Planar Mo2C: Role of Mo Diffusion. 2D Mater 2022, 9, No. 015039.
- (6) Shehzad, M. A.; Lee, Y.-S.; Cheng, M.; Lebedev, D.; Tyner, A. C.; Das, P. M.; Gao, Z.; Goswami, P.; Dos Reis, R.; Hersam, M. C.; Chen, X.; Dravid, V. P. Vapor–Liquid Assisted Chemical Vapor Deposition of Cu2X Materials. 2D Mater 2022, 9, No. 045013.
- (7) Feng, J.; Gao, H.; Li, T.; Tan, X.; Xu, P.; Li, M.; He, L.; Ma, D. Lattice-Matched Metal—Semiconductor Heterointerface in Monolayer Cu2Te. ACS Nano 2021, 15, 3415—3422.
- (8) Mallick, M. M.; Vitta, S. Realizing High Figure-of-Merit in Cu2Te Using a Combination of Doping, Hierarchical Structure, and Simple Processing. *J. Appl. Phys.* **2017**, *122*, No. 024903.
- (9) Mukherjee, S.; Chetty, R.; Madduri, P. V. P.; Nayak, A. K.; Wojciechowski, K.; Ghosh, T.; Chattopadhyay, K.; Suwas, S.; Mallik, R. C. Investigation on the Structure and Thermoelectric Properties of CuxTe Binary Compounds. *Dalton Trans.* **2019**, *48*, 1040–1050.
- (10) Pandey, J.; Mukherjee, S.; Rawat, D.; Athar, S.; Rana, K. S.; Mallik, R. C.; Soni, A. Raman Spectroscopy Study of Phonon Liquid Electron Crystal in Copper Deficient Superionic Thermoelectric Cu2–XTe. ACS Appl. Energy Mater. 2020, 3, 2175–2181.
- (11) Park, D.; Ju, H.; Oh, T.; Kim, J. Facile Fabrication of One-Dimensional Te/Cu2Te Nanorod Composites with Improved Thermoelectric Power Factor and Low Thermal Conductivity. *Sci. Rep.* **2018**, *8*, 18082.
- (12) Qiu, Y.; Liu, Y.; Ye, J.; Li, J.; Lian, L. Synergistic Optimization of Carrier Transport and Thermal Conductivity in Sn-Doped Cu2Te. *J. Mater. Chem. A* **2018**, *6*, 18928–18937.
- (13) Lee, D. J.; Mohan Kumar, G.; Ganesh, V.; Jeon, H. C.; Kim, D. Y.; Kang, T. W.; Ilanchezhiyan, P. Novel Nanoarchitectured Cu2Te as a Photocathodes for Photoelectrochemical Water Splitting Applications. *Nanomaterials* **2022**, *12*, 3192.
- (14) Li, Q.; Rao, H.; Ma, X.; Mei, H.; Zhao, Z.; Gong, W.; Camposeo, A.; Pisignano, D.; Yang, X. Unusual Red Light Emission from Nonmetallic Cu2Te Microdisk for Laser and SERS Applications. *Adv. Opt. Mater.* **2022**, *10*, 2101976.
- (15) Pollmann, E.; Maas, A.; Marnold, D.; Hucht, A.; Neubieser, R.-M.; Stief, M.; Madauß, L.; Schleberger, M. Dynamic Growth/Etching Model for the Synthesis of Two-Dimensional Transition Metal Dichalcogenides via Chemical Vapour Deposition. 2D Mater 2022, 9, No. 035001.
- (16) Schröder, U. A.; Grånäs, E.; Gerber, T.; Arman, M. A.; Martínez-Galera, A. J.; Schulte, K.; Andersen, J. N.; Knudsen, J.; Michely, T. Etching of Graphene on Ir(111) with Molecular Oxygen. *Carbon* **2016**, *96*, 320–331.

- (17) Wang, J.; Xu, X.; Qiao, R.; Liang, J.; Liu, C.; Zheng, B.; Liu, L.; Gao, P.; Jiao, Q.; Yu, D.; Zhao, Y.; Liu, K. Visualizing Grain Boundaries in Monolayer MoSe2 Using Mild H2O Vapor Etching. *Nano Res.* **2018**, *11*, 4082–4089.
- (18) Zhang, Y.; Li, Z.; Kim, P.; Zhang, L.; Zhou, C. Anisotropic Hydrogen Etching of Chemical Vapor Deposited Graphene. *ACS Nano* **2012**, *6*, 126–132.
- (19) Yamamoto, M.; Einstein, T. L.; Fuhrer, M. S.; Cullen, W. G. Anisotropic Etching of Atomically Thin MoS2. *J. Phys. Chem. C* **2013**, 117, 25643–25649.
- (20) Li, H.; Wu, H.; Yuan, S.; Qian, H. Synthesis and Characterization of Vertically Standing MoS2 Nanosheets. *Sci. Rep.* **2016**, *6*, 21171
- (21) Ye, H.; Zhou, J.; Er, D.; Price, C. C.; Yu, Z.; Liu, Y.; Lowengrub, J.; Lou, J.; Liu, Z.; Shenoy, V. B. Toward a Mechanistic Understanding of Vertical Growth of van Der Waals Stacked 2D Materials: A Multiscale Model and Experiments. *ACS Nano* **2017**, *11*, 12780–12788.
- (22) McCann, S. D.; Stahl, S. S. Copper-Catalyzed Aerobic Oxidations of Organic Molecules: Pathways for Two-Electron Oxidation with a Four-Electron Oxidant and a One-Electron Redox-Active Catalyst. *Acc. Chem. Res.* **2015**, *48*, 1756–1766.
- (23) Gravel, E.; Doris, E. Fullerenes Make Copper Catalysis Better. *Science* **2022**, *376*, 242–243.
- (24) Li, J.; Ozden, A.; Wan, M.; Hu, Y.; Li, F.; Wang, Y.; Zamani, R. R.; Ren, D.; Wang, Z.; Xu, Y.; Nam, D.-H.; Wicks, J.; Chen, B.; Wang, X.; Luo, M.; Graetzel, M.; Che, F.; Sargent, E. H.; Sinton, D. Silica-Copper Catalyst Interfaces Enable Carbon-Carbon Coupling towards Ethylene Electrosynthesis. *Nat. Commun.* **2021**, *12*, 2808.
- (25) Han, C.; Bai, Y.; Sun, Q.; Zhang, S.; Li, Z.; Wang, L.; Dou, S. Ambient Aqueous Growth of Cu2Te Nanostructures with Excellent Electrocatalytic Activity toward Sulfide Redox Shuttles. *Adv. Sci.* **2016**, 3, 1500350.
- (26) Li, B.; Huang, L.; Zhao, G.; Wei, Z.; Dong, H.; Hu, W.; Wang, L.-W.; Li, J. Large-Size 2D β -Cu2S Nanosheets with Giant Phase Transition Temperature Lowering (120 K) Synthesized by a Novel Method of Super-Cooling Chemical-Vapor-Deposition. *Adv. Mater.* **2016**, 28, 8271–8276.
- (27) Qiu, Y.; Ye, J.; Liu, Y.; Yang, X. Facile Rapid Synthesis of a Nanocrystalline Cu2Te Multi-Phase Transition Material and Its Thermoelectric Performance. RSC Adv. 2017, 7, 22558–22566.
- (28) Zhang, Y.; Zhang, Z.; Liu, W.; Zheng, Y.; Wu, Y.; Su, J.; Liu, N.; Gao, Y. In Situ Insight into Thermally-Induced Reversible Transitions of Crystal Structure and Photoluminescence Properties in Cu2Te Nanoplate. *J. Mater. Chem. A* **2021**, *9*, 26095–26104.
- (29) Blachnik, R.; Lasocka, M.; Walbrecht, U. The System Copper-Tellurium. *J. Solid State Chem.* **1983**, 48, 431–438.
- (30) Pashinkin, A. S.; Fedorov, V. A. Phase Equilibria in the Cu-Te System. 2003, 39 (6), 16, DOI: 10.1023/A:1024003932461.
- (31) Asadov, Y. G.; Asadova, S. Y.; Movlamverdieva, A. I.; Isaev, F. K. Effect of Zinc Doping on the Phase-Transition Temperatures of Cu2Te. *Inorg. Mater.* **2002**, *38*, 1103–1108.
- (32) Gurarslan, A.; Yu, Y.; Su, L.; Yu, Y.; Suarez, F.; Yao, S.; Zhu, Y.; Ozturk, M.; Zhang, Y.; Cao, L. Surface-Energy-Assisted Perfect Transfer of Centimeter-Scale Monolayer and Few-Layer MoS2 Films onto Arbitrary Substrates. *ACS Nano* **2014**, *8*, 11522–11528.
- (33) Sirusi, A. A.; Page, A.; Uher, C.; Ross, J. H. NMR Study of Vacancy and Structure-Induced Changes in Cu2-XTe. *J. Phys. Chem. Solids* **2017**, *106*, 52–57.
- (34) Salmón-Gamboa, J. U.; Barajas-Aguilar, A. H.; Ruiz-Ortega, L. I.; Garay-Tapia, A. M.; Jiménez-Sandoval, S. J. Vibrational and Electrical Properties of Cu2—xTe Films: Experimental Data and First Principle Calculations. *Sci. Rep.* **2018**, *8*, 8093.
- (35) Muhunthan, N.; Singh, O. P.; Toutam, V.; Singh, V. N. Electrical Characterization of Grain Boundaries of CZTS Thin Films Using Conductive Atomic Force Microscopy Techniques. *Mater. Res. Bull.* **2015**, *70*, 373–378.
- (36) Kim, G. Y.; Jeong, A. R.; Kim, J. R.; Jo, W.; Son, D.-H.; Kim, D.-H.; Kang, J.-K. Surface Potential on Grain Boundaries and

Intragrains of Highly Efficient Cu2ZnSn(S,Se)4 Thin-Films Grown by Two-Step Sputtering Process. Sol. Energy Mater. Sol. Cells 2014, 127, 129–135.

- (37) Hu, B.; Ago, H.; Ito, Y.; Kawahara, K.; Tsuji, M.; Magome, E.; Sumitani, K.; Mizuta, N.; Ikeda, K. I.; Mizuno, S. Epitaxial Growth of Large-Area Single-Layer Graphene over Cu(1 1 1)/Sapphire by Atmospheric Pressure CVD. *Carbon* **2012**, *50*, 57–65.
- (38) Shen, Y.; Liang, L.; Zhang, S.; Huang, D.; Zhang, J.; Xu, S.; Liang, C.; Xu, W. Organelle-Targeting Surface-Enhanced Raman Scattering (SERS) Nanosensors for Subcellular PH Sensing. *Nanoscale* **2018**, *10*, 1622–1630.
- (39) Shi, Y.; Li, H.; Li, L.-J. Recent Advances in Controlled Synthesis of Two-Dimensional Transition Metal Dichalcogenides via Vapour Deposition Techniques. *Chem. Soc. Rev.* **2015**, *44*, 2744–2756.
- (40) Wang, Z.; Li, Q.; Xu, H.; Dahl-Petersen, C.; Yang, Q.; Cheng, D.; Cao, D.; Besenbacher, F.; Lauritsen, J. V.; Helveg, S.; Dong, M. Controllable Etching of MoS2 Basal Planes for Enhanced Hydrogen Evolution through the Formation of Active Edge Sites. *Nano Energy* **2018**, *49*, 634–643.
- (41) Ionescu, R.; George, A.; Ruiz, I.; Favors, Z.; Mutlu, Z.; Liu, C.; Ahmed, K.; Wu, R.; Jeong, J. S.; Zavala, L.; Mkhoyan, K. A.; Ozkan, M.; Ozkan, C. S. Oxygen Etching of Thick MoS2 Films. *Chem. Commun.* **2014**, *50*, 11226–11229.
- (42) Nakano, M.; Wang, Y.; Kashiwabara, Y.; Matsuoka, H.; Iwasa, Y. Layer-by-Layer Epitaxial Growth of Scalable WSe2 on Sapphire by Molecular Beam Epitaxy. *Nano Lett.* **2017**, *17*, 5595–5599.
- (43) Dong, J.; Zhang, L.; Dai, X.; Ding, F. The Epitaxy of 2D Materials Growth. *Nat. Commun.* 2020, 11, 5862.

☐ Recommended by ACS

Synthesizing Mono- and Bimetallic 2D Selenophosphates Using a P₂Se₅ Reactive Flux

Eric K. Qian, Mercouri G. Kanatzidis, et al.

APRIL 25, 2023

CHEMISTRY OF MATERIALS

READ 🗹

A Low-Temperature Growth Mechanism for Chalcogenide Perovskites

Ruiquan Yang, Charles J. Hages, et al.

JUNE 06, 2023

CHEMISTRY OF MATERIALS

READ 🗹

Is Cu₃, P a Semiconductor, a Metal, or a Semimetal?

Andrea Crovetto, Andriy Zakutayev, et al.

JANUARY 25, 2023

CHEMISTRY OF MATERIALS

READ 🗹

Cation Segregation in Alloyed Thiophosphates Fe_{2-x}Co_xP₂S₆

Matthew Cheng, Vinayak P. Dravid, et al.

FEBRUARY 02, 2023

CHEMISTRY OF MATERIALS

READ 🗹

Get More Suggestions >